Next-generation crossover-free quantum Hall arrays with superconducting interconnections

Next-generation crossover-free quantum Hall arrays with superconducting interconnections

Mattias Kruskopf[1,2], Albert F. Rigosi[1], Alireza R. Panna[1], Martina Marzano[4], Dinesh Patel[3], Hanbyul Jin[1,2], David B. Newell[1], and Randolph E. Elmquist[1]

[1]National Institute of Standards and Technology (NIST), Gaithersburg, MD 20899, USA

[2]Joint Quantum Institute, University of Maryland, College Park, MD 20742, USA

[3]Department of Physics, National Taiwan University, Taipei 10617, Taiwan

[4]Politecnico di Torino, Istituto Nazionale di Ricerca Metrologica, Turin, Italy

E-mail: mattias.kruskopf@nist.gov, albert.rigosi@nist.gov, alireza.panna@nist.gov, m.marzano@inrim.it, dkpjnp@gmail.com, hanbyul.jin@nist.gov, david.newell@nist.gov and randolph.elmquist@nist.gov

Keywords: quantum Hall effect, quantized Hall array resistance standards, epitaxial graphene, superconducting contacts, multiple connection, split contacts

Abstract: This work presents precision measurements of quantized Hall array resistance devices using superconducting, crossover-free, multiple interconnections as well as graphene split-contacts. These new techniques successfully eliminate the accumulation of internal resistances and leakage currents that typically occur at interconnections and crossing leads between interconnected devices. As a result, a scalable quantized Hall resistance array is obtained with a nominal value that is as precise and stable as that from single-element quantized Hall resistance standards.

1. Introduction

Although the first graphene samples were isolated as micrometer-size flakes and found to have favorable electrical and optical properties,[1–5], more recently, high-quality and centimeter-scale graphene has been obtained through epitaxial growth on silicon carbide (SiC) [6–9]. The epitaxial graphene (EG) growth has improved to the point that one can realize devices suitable for general applications, like larger scale electronics, and more specialized applications, such as quantized Hall resistance (QHR) standards [9–17].

Limitations of reliable access to quantum Hall resistance plateaus other than $R_H = R_K/2 = h/2e^2$, where R_H is the Hall resistance and R_K is the von Klitzing constant, have motivated the development of quantum Hall array resistance standards (QHARS) based on series and in parallel connected devices [18–20]. These next-generation quantum resistance devices show promise in fulfilling the requirement of scalability for future applications in metrology. One issue for these scalable resistance networks, based on many Hall bar elements, is that they may suffer from accumulated internal resistances and Hall resistance contributions at thin-film metal contacts and interconnections. In addition, the crossover of electrical connections between Hall elements introduce other difficulties such as possible leakage currents through the dielectric where the voltage terminals need to cross the current path. Finally, because of limited chip mounting options, it is impossible to realize longitudinal resistance measurements as recommended in metrological guidelines for the QHR [21]. These challenges are the reason why state-of-the-art QHARS devices often cannot reach the level of quantization needed for resistance metrology.

In this work, we present new EG-based QHARS device design approaches to minimize the error contributions of undesired resistances at contacts and interconnections and ensure precise resistance quantization for series-parallel networks. The applied split-contact geometry and superconducting interconnections ensure minimum deviation from the nominal resistance value on the order of 10^{-9}. Furthermore, new quantization criteria are applied to verify the quantization of these resistance networks as a whole rather than by the characterization of single Hall devices in addition to previously discussed concepts [22,23].

2. Device preparation and characterization

2.1. Sample and contact design

Figure 1(a) shows the sample design based on six Hall bars (light grey), superconducting interconnections and contacts (dark grey), and the positions of the bonding wires (blue) that were used for the four-terminal resistance measurements. Each Hall bar was contacted by a multiple interconnection [20,24] that was optimized for a specific magnetic field direction such that the hot-spot forms in the lower left and upper right corner of each device as indicated in Figure 1(b). The device fabrication started with the deposition of a Pd/Au layer onto the EG. After the EG/Pd/Au layer was structured into the Hall bar shape by argon plasma etching, it was contacted with a ≈ 320 nm thick NbTiN layer and capped with a ≈ 30 nm thick Pt layer to prevent surface oxidation. A detailed description of the individual fabrication steps is given in a previous work [25]. The confocal laser scanning microscope (CLSM) image of the finished device is given in Figure 1(b). Before the device was wire-bonded onto a chip carrier, covalent $Cr(CO)_3$ functionalization was used to adjust the charge carrier density of the device as explained in Section 2.2. A previous work shows that by integrating the principle of the Delahaye triple-series interconnection for QHR devices into a single contact (by means of split contacts shown in

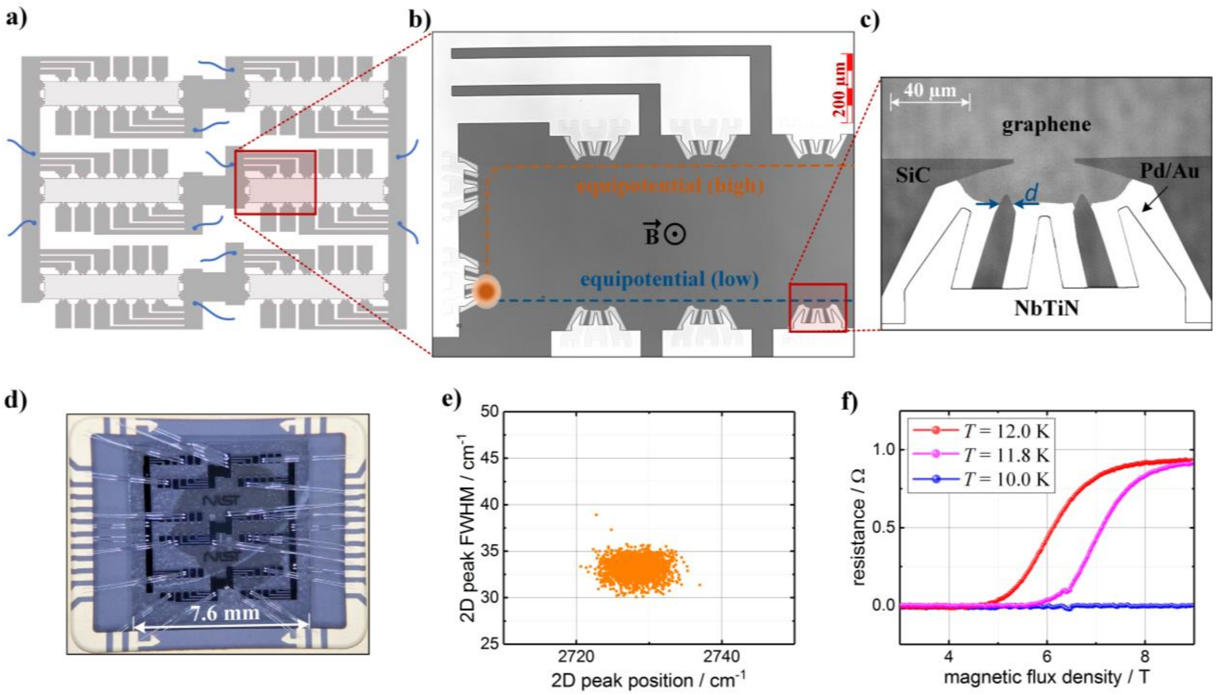

Figure 1. Device design and sample characteristics. (a) The sample design of the graphene quantized Hall array resistance device shows the interconnections (dark grey) of the individual QHR elements (light grey) and the positions of the bonding wires that were used for the measurement (blue). The red inset box marks the region shown in (b). (b) Confocal laser scanning microscope (CLSM) image of a graphene Hall bar device in the source/drain contact region using a multiple connection and superconducting split contacts. (c) CLSM image in the region of the graphene/NbTiN split contact shows the design used to realize negligible contact resistances. (d) The photo shows the contacted device (7.6 mm × 7.6 mm) mounted on a 32-pin chip carrier. (e) The scatter plot of Raman graphene 2D (G\`) peak characteristics was evaluated from 50 µm × 50 µm area maps and shows a typical distribution of the FWHM and the peak position over centimeter-scale areas. (f) The graph shows the vanishing resistance across a superconducting element of the device for different temperatures and magnetic flux densities. The high critical magnetic field of the NbTiN superconductor ensures superconductivity even at $T \approx 10$ K for magnetic flux densities $B > 9$ T. At $B = 0$ T, the typical critical transition temperature is around 12.5 K.

Figure 1(b) and Figure 1(c)), the resulting contact resistance in the quantum Hall regime is reduced to a level of 100 µΩ or less [25]. The vanishing contact resistance is the result of the current flowing through mainly one branch of the split-contact, with each other branch experiencing a proportion of current that is smaller than the last. Thus, the connection voltage drop quickly approaches zero, bringing the superconductor to the potential of the quantized two-dimensional electron gas (2DEG). The condition for the branches to act as separate charge carrier reservoirs in the quantum Hall regime is separation by a minimum distance d, which must be larger than the inelastic scattering length of the charge carrier [26]. It is safe to assume that the condition is fulfilled for the distance $d \geq 5$ µm indicated in Figure 1(c) between neighboring branches since inelastic scattering occurs at sub-micron length scales [27,28]. Additionally, the design accounts for the prevention of Andreev reflections that may occur at EG/superconductor interfaces and can lead to deviations of the Hall resistance from the nominal value [29–32]. As demonstrated in Figure 1(c), a several micrometer-wide Pd/Au stripe separates the EG edge from the NbTiN superconductor such that Andreev effects cannot occur. Figure 1(d) shows the array device mounted in a 32-pin leadless chip carrier (LCC03204) that was used for the pre-characterization. Precision measurements of the same sample were performed afterward using a transistor outline (TO-8) package.

2.2. Graphene growth, device fabrication and carrier density control

EG was obtained by thermally decomposing the Si-face of 4H-SiC(0001) semi-insulating substrates having a miscut of less than 0.10°. Substrates were first diced from a 4-inch wafer into squares with sides measuring 22.8 mm × 22.8 mm, cleaned by a piranha etch, immersed into diluted hydrofluoric acid, and surface-treated with polymer adsorbates for polymer-assisted sublimation growth (PASG) [8,9]. PASG involved spin coating a weak solution of 0.2 % (by volume) AZ5214E polymer in isopropanol. Prior to EG growth, the prepared substrates were then placed on a slab of polished graphite with the Si-face in direct contact with the slab for face-to-graphite growth [13,33]. The combination of the face-to-graphite growth and PASG methods supports the formation of a uniform surface morphology and suppresses the formation of high substrate steps and bilayer domains. Reducing the SiC terrace height to a sub-nanometer level is important since it reduces variations of the doping level, the number of scattering centers, and strain caused by local detachment of the graphene layer at the edges of the terraces [34–37]. The annealing process at 1900 °C was performed in argon at atmospheric pressure with a graphite-lined resistive-element furnace. After growth, the EG quality was assessed using CLSM and optical microscopy, both being convenient and preparation-free methods for rapid identification of successful large-area growths [38].

Raman spectroscopy was performed to verify that the EG was undamaged before and after the functionalization process. Spectra were collected with a spectrometer using a 532.2 nm wavelength excitation laser source and a backscattering configuration. The spot size was about 1 µm, the acquisition times were 2 s, the laser power was 25 mW power, and the optical path included a 50 × objective and 600 mm^{-1} gratings. Square Raman maps were collected with step sizes of 0.5 µm in a 100 by 100 raster-style grid. The large-scale quality of the EG was assessed by monitoring only the 2D (G`) peak and its Raman shift, full width at half maximum (FWHM), and spatial location on the device. The 2D (G`) peak quantities are summarized in Figure 1 (e), with average FWHM of 33.16 cm^{-1} ± 0.93 cm^{-1} and average peak position of 2728.07 cm^{-1} ± 3.36 cm^{-1} (all uncertainties represent 1σ deviations). Figure 1 (d) shows a photo of the measured device which was fabricated using NbTiN contacts and interconnections.

Functionalization of EG with $Cr(CO)_3$ was performed to have improved control over the carrier density, as it had been demonstrated in other reports [39–44]. To begin the functionalization process, the completed EG device was loaded onto a phosphor-bronze boat filled with approximately 100 mg of crystalline $Cr(CO)_6$ (chromium hexacarbonyl) and placed within a homemade vacuum furnace. The deposition steps (well-documented in Ref. [44]) resulted in ring-centered $Cr(CO)_3$ functionalization. By functionalizing the EG surface, the electron doping was reduced to a carrier density below 10^{11} cm^{-2} and produced limited drift of the carrier density in air. To adjust the carrier density to the level of about 2×10^{11} cm^{-2} for the measurement, the sample was annealed at 355 K for about 20 minutes in vacuum and was cooled down immediately afterward.

2.3. Assessment of NbTiN properties

The measurement temperature and applied magnetic flux densities need to be far below the critical properties of the superconductor to allow voltage and current terminals to be the same by using multiple interconnections without crossing leads. This is not only important to avoid undesired ohmic resistance contributions but also to avoid the occurrence of non-zero Hall fluctuations at interconnections [45,46].

To assess the most important properties of the NbTiN superconductor, the four-wire resistance across a superconducting element of the device was monitored as a function of the magnetic flux density and temperature. Figure 1(f) shows that the resistance vanishes at a temperature of $T = 10$ K and magnetic flux densities up to $B = 9$ T. At this temperature the critical field is likely to be higher since a breakdown of the superconductivity was only observed above 11.5 K for the system's highest available magnetic flux density of $B = 9$ T. At zero magnetic flux density, the typical critical temperature of this superconductor is $T \approx 12.5$ K.

3. Results and discussion

Under the assumption of negligible resistance contributions from contacts and superconducting strip lines, the quantum Hall array device introduced in Figure 1 provides access to several measurement configurations resulting in different nominal resistance values. Here we focus on only those configurations in which the current splits equally among two or more paths and that provide access to null measurements that may be used to check for the uniformity and quantization of the resistance array. This characterization is complementary to the comparison to a calibrated 100 Ω standard resistor using a cryogenic current comparator (CCC) resistance bridge.

To precisely determine the array resistance values using the CCC bridge, a NIST 100 Ω standard resistor (Electro-Scientific Industries SR102) was used. The standard resistor has a well-known linear drift rate and was calibrated about 100 days prior to the characterization of the array device using a GaAs-AlGaAs quantized Hall resistance standard.

3.1. Measurement configuration 1 results, $R = 2/6\ R_K \approx 8604\ \Omega$

Figure 2(a) shows the first configuration of three parallel pairs of series-connected quantized Hall devices with a resulting nominal resistance of $R_{a,b} = U_{a,b}/I_{a,b} = 2/6\ R_K \approx 8604\ \Omega$. The voltage differences $U_{1,2}$, $U_{1,3}$, $U_{2,3}$ at the terminals "1, 2, 3" in the center of the sample are monitored to detect a breakdown of the resistance quantization.

Figure 2(b) shows lock-in measurements of the magnetic field dependence of the resistance $R_{a,b}$ with a symmetrical behavior at low fields below ±5 T and a wide resistance plateau beyond ± 5 T. Due to similar carrier densities of the devices, the potential differences $U_{1,2}$, $U_{1,3}$, and $U_{2,3}$ show Shubnikov-de Haas oscillations at lower fields and approach zero for ± 5 T.

Precision measurements of the potential differences at $B = 9$ T shown in Figure 2(c) were collected using a nanovoltmeter (EM N11) and a NIST-built ramping voltage source that is normally used in a CCC resistance bridge system [47]. The voltage source was operated at $U_{SD} = U_{a,b} = 1.26$ V to provide a stable current of $I_{a,b} \approx 146$ µA, or $I_{\mathrm{SD}} \approx 49$ µA through each of the six QHR devices. Measurements were performed by recording at least ten points, each using direct current (dc) reversal cycles to eliminate thermal voltages with a ramp time = 1 s, settle

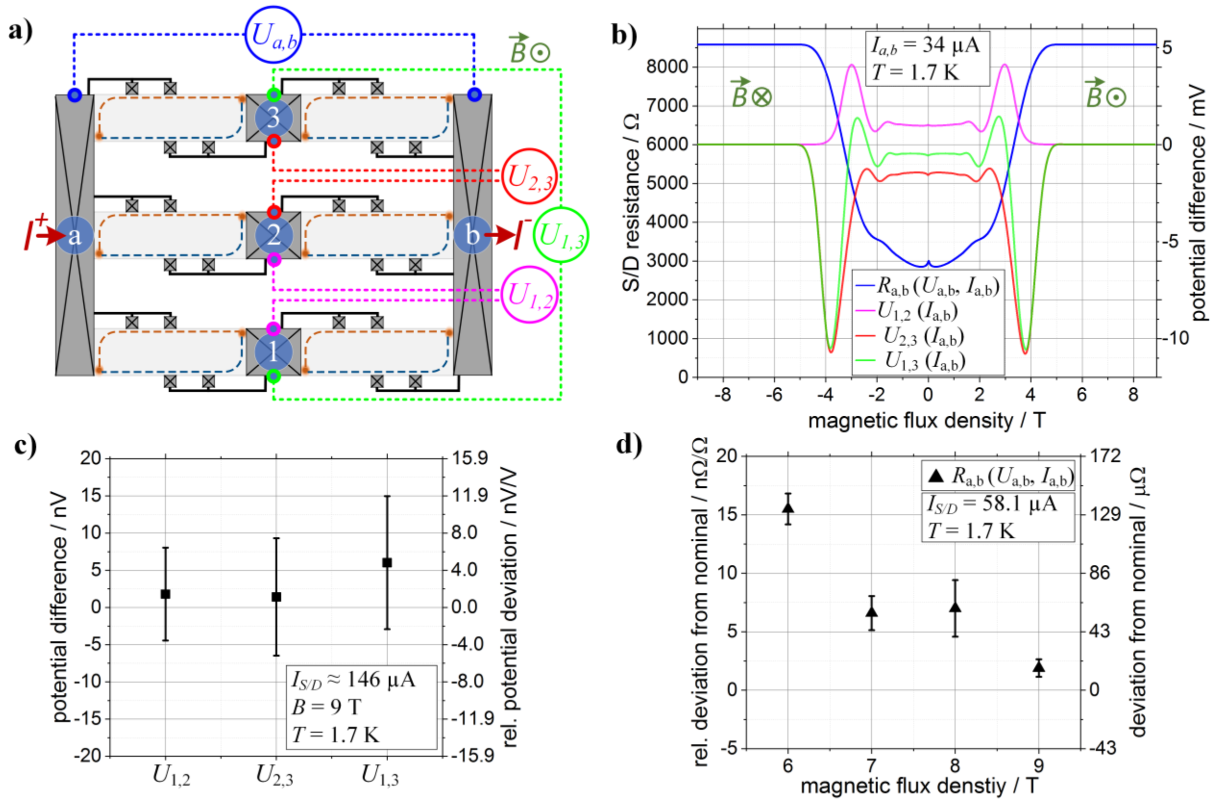

Figure 2. Measurement configuration with a nominal resistance value of $R_{a/b} = 2/6\ R_K \approx 8604\ \Omega$. (a) The simplified schematic of the array device shows the measurement configuration for the characterization of the source/drain (SD) resistance of $R_{a/b} = U_{a,b}/I_{a,b}$ and the potential differences $U_{1,2}$, $U_{2,3}$ and $U_{1,3}$. The indicated high (red) and low (blue) equipotential lines describe the case for a quantized device at positive flux densities. (b) The SD resistance and the potential differences U_i at the center locations 1,2,3 as a function of the magnetic flux density show wide plateaus for $B > 5$ T. (c) Measurements at $B = 9$ T show that once resistance quantization is obtained, the voltage differences at the center locations 1,2,3 become zero within the measurement uncertainty and thus serve as a simple quantization check of the device. (d) The precision CCC comparison of $R_{a/b}$ with a 100 Ω standard resistor for $B = 9$ T shows a deviation of ≈ 2 nΩ/Ω from the expected nominal value.

time = 8 s and an integration time = 8 s. Additionally, each data point U_i in Figure 2(c) is composed of two measurement sets with reversed nanovoltmeter potential terminals such that $U_i = (U_i^{+-} - U_i^{-+})/2$ to reject constant voltage offsets that are typically < 10 nV. All three determined potential differences between the three parallel device branches with a mean value of 3.1 nV ± 7.6 nv were zero within the measurement uncertainty which indicates that all six devices were equal and thus almost certainly well quantized. To make measurements using different measurement conditions better comparable, the relative potential deviation $\delta U_{dev} = U_i/U_{SD}$ was determined resulting in a mean value of all three measurements of 2.5 nV/V ± 6.1 nV/V. This method achieves a metrological useful sensitivity to resistance differences below 10 nΩ/Ω with respect to a 12.9 kΩ resistor assuming a potential difference measurement with a statistical uncertainty < 10 nV and currents on the order of 100 µA.

A comparison of the QHARS and a 100 Ω standard resistor was realized using a binary cryogenic current comparator (BCCC) bridge [48]. Figure 2(d) shows the field-dependent

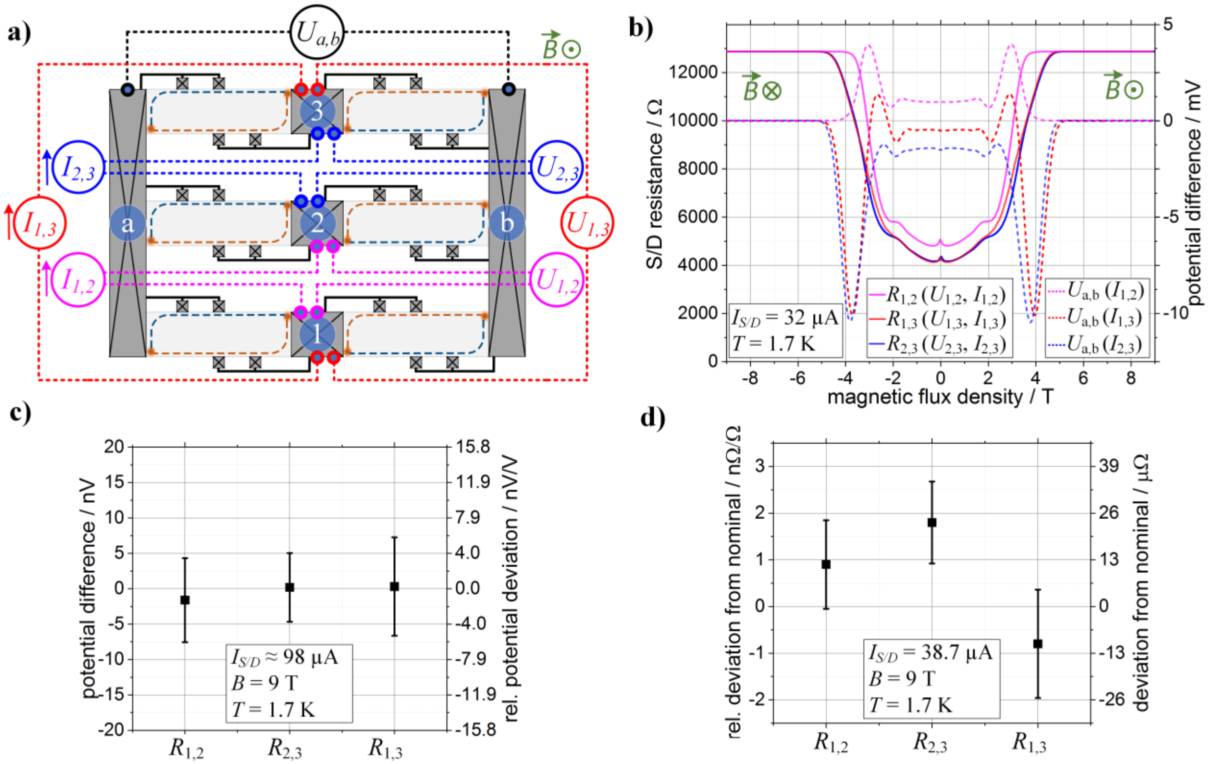

Figure 3. Measurement configuration with a nominal resistance value of $R_{1,2} = R_{2,3} = R_{1,3} = 1/2\ R_K \approx 12906\ \Omega$. (a) The simplified schematic of the array device shows the measurement configuration for the characterization of the source/drain (S/D) resistances $R_{1,2} = R_{2,3} = R_{1,3}$ and the corresponding potential differences $U_{a,b}$. The indicated high (red) and low (blue) equipotential lines describe the case for a quantized device at positive flux densities. (b) The SD resistances as well as corresponding potential differences between port "a" and "b" as a function of the magnetic flux density show wide plateaus for $B > 5$ T. (c) At $B = 9$ T, the voltage differences $U_{a,b}$ for each of the three SD resistances $R_{1,2}$, $R_{2,3}$, $R_{1,3}$ are zero to within the measurement uncertainty and thus serve as a simple quantization check of the device. (d) The precision CCC comparison of the three SD resistances with a 100 Ω standard resistor at 9 T show near-zero deviations from the expected nominal value of $R_{1,2} = R_{2,3} = R_{1,3}$.

deviation from the nominal resistance value $R_{a,b} = 2/6\ R_K$ as a function of the magnetic flux density between $B = 6$ T and $B = 9$ T. The data points for $B \geq 7$ T have a relative deviation well below 10 nΩ/Ω with the lowest value being 1.9 nΩ/Ω ± 0.75 nΩ/Ω at $B = 9$ T. The larger uncertainties of the measurements at 8 T, 7 T, and 6 T are related to the lower number of collected measurements of 25 points compared to 50 points at 9 T. The error bars shown in Figure 2(d) only account for the type A ($k = 1$) uncertainties of the measurements.

3.2. Measurement configuration 2 results, $R = 1/2\ R_K \approx 12906\ \Omega$

In the second measurement set shown in Figure 3(a), the QHARS device was contacted such that only four out of the six devices contributed to the transport, creating a network with two parallel pairs of series-connected devices. This was achieved by using the terminals "1,2,3" as current terminals such that $R_{1,2} = R_{2,3} = R_{1,3}$ with a nominal value of $1/2\ R_K \approx 12906\ \Omega$. The terminals "a" and "b" were used to identify asymmetries in the device by monitoring the potential difference $U_{a,b}$.

Figure 3(b) shows the field dependence of $R_{1,2}$, $R_{2,3}$ and $R_{1,3}$ and their corresponding potential differences $U_{a,b}$ monitored with a lock-in measurement system within the range of available magnetic flux densities of $-9\ T \leq B \leq 9\ T$. Small differences in the charge carrier densities and low-field resistivities of the devices resulted in somewhat different onsets of the resistance plateaus at 1/2 $R_K \approx 12906\ \Omega$ around ±5 T. Measurements of $U_{a,b}$ in Figure 3(b) show that the potential differences of all three measurements with a mean value of -0.29 nV ± 4.7 nV are zero to within the measurement uncertainty and thus indicate the well quantization of all Hall elements.

The CCC resistance comparison of the QHARS against the same 100 Ω standard resistor in Figure 3(c) proves that all three resistances $R_{1,2}$, $R_{2,3}$ and $R_{1,3}$ were well quantized at 1/2 R_K with a deviation of ≈ ±2 nΩ/Ω.

4. Conclusions

We have demonstrated the fabrication and functionality of EG-based QHARS that provide variable resistances with excellent quantization properties resulting in deviations from its nominal value on the order of ± 2 nΩ/Ω. Additionally, the introduced relative potential deviation measurements between points of equal potential in the symmetric network design were successfully applied to verify the uniformity and quantization of the device. This technique does not require the assessment of individual devices and thus represents a straightforward quantization criterion of QHARS.

The reasons for the reported performance that matches that of single quantum Hall devices are the crossover-free, superconducting NbTiN interconnections that eliminate ohmic resistance contributions and Hall fluctuations as well as the applied split-contacts with minimum contact resistances. By presenting a novel way to simplify device interconnections without altering the quantized resistance value this work brings the development of QHARS to the next stage.

Author Contributions

M.K. and A.F.R have contributed equally to this manuscript. M.K., A.F.R., and R.E.E. developed the EG functionalization process. M.K., A.R.P., M.M., D.P., A.F.R., and H.J. performed transport measurements. M.K. produced the graphene samples and fabricated the devices. The manuscript was written through the contributions of all authors. All authors have given approval to the final version of the manuscript.

Acknowledgments

The work of D.P. at NIST was made possible by arrangement with C.-T. Liang of National Taiwan University, and the work of M.M. at NIST was made possible by arrangement with M. Ortolano of Politecnico di Torino and L. Callegaro of the Istituto Nazionale di Ricerca Metrologica, Turin, Italy. The authors would like to thank S. Schlamminger and A. Biacchi for their assistance during the internal review at NIST. Commercial equipment, instruments, and materials are identified in this paper in order to specify the experimental procedure adequately. Such identification is not intended to imply recommendation or endorsement by the National Institute of Standards and Technology or the United States government, nor is it intended to imply that the materials or equipment identified are necessarily the best available for the purpose.

References

[1] Geim A K and Novoselov K S 2007 The rise of graphene *Nat. Mater.* **6** 183–91

[2] Castro Neto A H, Guinea F, Peres N M R, Novoselov K S and Geim A K 2009 The electronic properties of graphene *Rev. Mod. Phys.* **81** 109–62

[3] Novoselov K S, Fal′ko V I, Colombo L, Gellert P R, Schwab M G and Kim K 2012 A roadmap for graphene *Nature* **490** 192–200

[4] Das Sarma S, Adam S, Hwang E H and Rossi E 2011 Electronic transport in two-dimensional graphene *Rev. Mod. Phys.* **83** 407–70

[5] Berger C, Song Z, Li T, Li X, Ogbazghi A Y, Feng R, Dai Z, Alexei N, Conrad M E H, First P N and De Heer W A 2004 Ultrathin epitaxial graphite: 2D electron gas properties and a route toward graphene-based nanoelectronics *J. Phys. Chem. B* **108** 19912–6

[6] Virojanadara C, Syväjarvi M, Yakimova R, Johansson L I, Zakharov A A and Balasubramanian T 2008 Homogeneous large-area graphene layer growth on SiC(0001) *Phys. Rev. B* **78** 245403

[7] Emtsev K V., Bostwick A, Horn K, Jobst J, Kellogg G L, Ley L, McChesney J L, Ohta T, Reshanov S A, Röhrl J, Rotenberg E, Schmid A K, Waldmann D, Weber H B and Seyller T 2009 Towards wafer-size graphene layers by atmospheric pressure graphitization of silicon carbide *Nat. Mater.* **8** 203–7

[8] Kruskopf M, Pakdehi D M, Pierz K, Wundrack S, Stosch R, Dziomba T, Götz M, Baringhaus J, Aprojanz J, Tegenkamp C, Lidzba J, Seyller T, Hohls F, Ahlers F J and Schumacher H W 2016 Comeback of epitaxial graphene for electronics: large-area growth of bilayer-free graphene on SiC *2D Mater.* **3** 041002

[9] Kruskopf M and Elmquist R E 2018 Epitaxial graphene for quantum resistance metrology *Metrologia* **55** R27–36

[10] Janssen T J B M, Tzalenchuk A, Yakimova R, Kubatkin S, Lara-Avila S, Kopylov S and Fal'ko V I 2011 Anomalously strong pinning of the filling factor ν=2 in epitaxial graphene *Phys. Rev. B* **83** 233402

[11] Ribeiro-Palau R, Lafont F, Brun-Picard J, Kazazis D, Michon A, Cheynis F, Couturaud O, Consejo C, Jouault B, Poirier W and Schopfer F 2015 Quantum Hall resistance standard in graphene devices under relaxed experimental conditions *Nat. Nanotechnol.* **10** 965–71

[12] Tzalenchuk A, Lara-Avila S, Kalaboukhov A, Paolillo S, Syväjärvi M, Yakimova R, Kazakova O, Janssen T J B M, Fal'ko V and Kubatkin S 2010 Towards a quantum resistance standard based on epitaxial graphene *Nat. Nanotechnol.* **5** 186–9

[13] Real M A, Lass E A, Liu F-H, Shen T, Jones G R, Soons J A, Newell D B, Davydov A V. and Elmquist R E 2013 Graphene Epitaxial Growth on SiC(0001) for Resistance Standards *IEEE Trans. Instrum. Meas.* **62** 1454–60

[14] Lafont F, Ribeiro-Palau R, Kazazis D, Michon A, Couturaud O, Consejo C, Chassagne T, Zielinski M, Portail M, Jouault B, Schopfer F and Poirier W 2015 Quantum hall resistance standards from graphene grown by chemical vapour deposition on silicon carbide *Nat. Commun.* **6** 1–10

[15] Janssen T J B M, Rozhko S, Antonov I, Tzalenchuk A, Williams J M, Melhem Z, He H, Lara-Avila S, Kubatkin S and Yakimova R 2015 Operation of graphene quantum Hall resistance standard in a cryogen-free table-top system *2D Mater.* **2** 035015

[16] Jeckelmann B and Jeanneret B 2001 The quantum Hall effect as an electrical resistance standard *Reports Prog. Phys.* **64** 1603–55
[17] Rigosi A F, Panna A R, Payagala S U, Kruskopf M, Kraft M E, Jones G R, Wu B-Y, Lee H-Y, Yang Y, Hu J, Jarrett D G, Newell D B and Elmquist R E 2019 Graphene Devices for Tabletop and High-Current Quantized Hall Resistance Standards *IEEE Trans. Instrum. Meas.* **68** 1870–8
[18] Novikov S, Lebedeva N, Hämäläinen J, Iisakka I, Immonen P, Manninen A J and Satrapinski A 2016 Mini array of quantum Hall devices based on epitaxial graphene *J. Appl. Phys.* **119** 174504
[19] Lartsev A, Lara-Avila S, Danilov A, Kubatkin S, Tzalenchuk A and Yakimova R 2015 A prototype of R K /200 quantum Hall array resistance standard on epitaxial graphene *J. Appl. Phys.* **118** 044506
[20] Delahaye F 1993 Series and parallel connection of multiterminal quantum Hall-effect devices *J. Appl. Phys.* **73** 7914–20
[21] Delahaye F and Jeckelmann B 2003 Revised technical guidelines for reliable dc measurements of the quantized Hall resistance *Metrologia* **40** 217–23
[22] Poirier W, Bounouh A, Piquemal F and André J P 2004 A new generation of QHARS: discussion about the technical criteria for quantization *Metrologia* **41** 285–94
[23] Konemann J, Ahlers F-J, Pesel E, Pierz K and Schumacher H W 2011 Magnetic Field Reversible Serial Quantum Hall Arrays *IEEE Trans. Instrum. Meas.* **60** 2512–6
[24] Jeffery A, Elmquist R E and Cage M E 1995 Precision tests of quantum hall effect device DC equivalent circuit using double-series and triple-series connections *J. Res. Natl. Inst. Stand. Technol.* **100** 677
[25] Kruskopf M, Rigosi A F, Panna A R, Patel D K, Jin H, Marzano M, Berilla M, Newell D B and Elmquist R E 2019 Two-terminal and multi-terminal designs for next generation quantized Hall resistance standards: contact material and geometry *Submitt. to Trans. Electron Devices*
[26] Büttiker M 1988 Absence of backscattering in the quantum Hall effect in multiprobe conductors *Phys. Rev. B* **38** 9375–89
[27] Baker A M R, Alexander-Webber J A, Altebaeumer T, Janssen T J B M, Tzalenchuk A, Lara-Avila S, Kubatkin S, Yakimova R, Lin C-T, Li L-J and Nicholas R J 2012 Weak localization scattering lengths in epitaxial, and CVD graphene *Phys. Rev. B* **86** 235441
[28] Drabińska A, Kamińska M, Wołoś A, Strupinski W, Wysmołek A, Bardyszewski W, Bożek R and Baranowski J M 2013 Enhancement of elastic and inelastic scattering lengths in quasi-free-standing graphene measured with contactless microwave spectroscopy *Phys. Rev. B* **88** 165413
[29] Sahu M R, Liu X, Paul A K, Das S, Raychaudhuri P, Jain J K and Das A 2018 Inter-Landau-level Andreev Reflection at the Dirac Point in a Graphene Quantum Hall State Coupled to a NbSe2 Superconductor *Phys. Rev. Lett.* **121** 086809
[30] Amet F, Ke C T, Borzenets I V., Wang J, Watanabe K, Taniguchi T, Deacon R S, Yamamoto M, Bomze Y, Tarucha S and Finkelstein G 2016 Supercurrent in the quantum Hall regime *Science (80-.).* **352** 966–9
[31] Rickhaus P, Weiss M, Marot L and Schönenberger C 2012 Quantum Hall Effect in Graphene with Superconducting Electrodes *Nano Lett.* **12** 1942–5
[32] Hou Z, Xing Y, Guo A-M and Sun Q-F 2016 Crossed Andreev effects in two-

dimensional quantum Hall systems *Phys. Rev. B* **94** 064516
[33] Yang Y, Cheng G, Mende P, Calizo I G, Feenstra R M, Chuang C, Liu C-W, Liu C, Jones G R, Hight Walker A R and Elmquist R E 2017 Epitaxial graphene homogeneity and quantum Hall effect in millimeter-scale devices *Carbon N. Y.* **115** 229–36
[34] Nagase M, Hibino H, Kagashima H and Yamaguchi H 2008 Local conductance measurement of few-layer graphene on SiC substrate using an integrated nanogap probe *J. Phys. Conf. Ser.* **100** 052006
[35] Low T, Perebeinos V, Tersoff J and Avouris P 2012 Deformation and Scattering in Graphene over Substrate Steps *Phys. Rev. Lett.* **108** 096601
[36] Willke P, Kotzott T, Pruschke T and Wenderoth M 2017 Magnetotransport on the nano scale *Nat. Commun.* **8** 15283
[37] Momeni Pakdehi D, Aprojanz J, Sinterhauf A, Pierz K, Kruskopf M, Willke P, Baringhaus J, Stöckmann J P, Traeger G A, Hohls F, Tegenkamp C, Wenderoth M, Ahlers F J and Schumacher H W 2018 Minimum Resistance Anisotropy of Epitaxial Graphene on SiC *ACS Appl. Mater. Interfaces* **10**
[38] Panchal V, Yang Y, Cheng G, Hu J, Kruskopf M, Liu C-I, Rigosi A F, Melios C, Hight Walker A R, Newell D B, Kazakova O and Elmquist R E 2018 Confocal laser scanning microscopy for rapid optical characterization of graphene *Commun. Phys.* **1** 83
[39] Bekyarova E, Sarkar S, Niyogi S, Itkis M E and Haddon R C 2012 Advances in the chemical modification of epitaxial graphene *J. Phys. D. Appl. Phys.* **45** 154009
[40] Che S, Jasuja K, Behura S K, Nguyen P, Sreeprasad T S and Berry V 2017 Retained Carrier-Mobility and Enhanced Plasmonic-Photovoltaics of Graphene via ring-centered η 6 Functionalization and Nanointerfacing *Nano Lett.* **17** 4381–9
[41] Chen M, Pekker A, Li W, Itkis M E, Haddon R C and Bekyarova E 2018 Organometallic chemistry of graphene: Photochemical complexation of graphene with group 6 transition metals *Carbon N. Y.* **129** 450–5
[42] Pinto H and Markevich A 2014 Electronic and electrochemical doping of graphene by surface adsorbates *Beilstein J. Nanotechnol.* **5** 1842–8
[43] Chuang C, Yang Y, Pookpanratana S, Hacker C A, Liang C-T and Elmquist R E 2017 Chemical-doping-driven crossover from graphene to "ordinary metal" in epitaxial graphene grown on SiC *Nanoscale* **9** 11537–44
[44] Rigosi A F, Kruskopf M, Hill H M, Jin H, Wu B-Y, Johnson P E, Zhang S, Berilla M, Hight Walker A R, Hacker C A, Newell D B and Elmquist R E 2019 Gateless and reversible Carrier density tunability in epitaxial graphene devices functionalized with chromium tricarbonyl *Carbon N. Y.* **142** 468–74
[45] Breznay N P and Kapitulnik A 2013 Observation of the ghost critical field for superconducting fluctuations in a disordered TaN thin film *Phys. Rev. B* **88** 104510
[46] Destraz D, Ilin K, Siegel M, Schilling A and Chang J 2017 Superconducting fluctuations in a thin NbN film probed by the Hall effect *Phys. Rev. B* **95** 1–6
[47] Hernandez-Marquez F L, Bierzychudek M E, Jones G R and Elmquist R E 2014 Precision high-value resistance scaling with a two-terminal cryogenic current comparator *Rev. Sci. Instrum.* **85** 044701
[48] Götz M and Drung D 2017 Stability and Performance of the Binary Compensation Unit for Cryogenic Current Comparator Bridges *IEEE Trans. Instrum. Meas.* **66** 1467–74